Aerospace Science and Technology 107 (2020) 106260

Contents lists available at ScienceDirect

Aerospace Science and Technology

www.elsevier.com/locate/aescte

Reverse jet parameters study on aerodynamic thermal uncertainty of a blunt body

Wei Zhang [a], Sheng Wang [a], Qiang Wang [b], Shengjun Ju [c], Chao Yan [a,*]

[a] National Key Laboratory of Computational Fluid Dynamics, Beihang University, Beijing 100191, China
[b] China Academy of Aerospace Aerodynamics, Beijing 100074, China
[c] Institute of Mechanics, Chinese Academy of Sciences, Beijing 100190, China

ARTICLE INFO

Article history:
Received 18 December 2019
Received in revised form 26 September 2020
Accepted 3 October 2020
Available online 13 October 2020
Communicated by Scott Morton

Keywords:
Aerodynamic thermal
Opposing jets
Parametric sensitivity analysis
Uncertainty quantification
Analysis of Variance
Non-Intrusive Polynomial Chaos

ABSTRACT

Adding head opposing jets is a common flow control approach to reduce the aerodynamic heating of hypersonic vehicles with blunt-shape head. However, interests of present studies are mostly focused on surface heating reduction originate from opposing jets only on single-and-determinate free incoming conditions, rather than that under existence of freestream perturbations, to the best of knowledge. In this work, two-layers research structure is formed to investigate the jet design parameters on surface thermal uncertainty with occurrence of free incoming perturbations. In the inner layer, the Polynomial Chaos method is applied for quantifying the surface thermal uncertainty, including the mean value and the standard deviation, under free incoming perturbations. In the outer layer, the Variance Analysis method is employed to describe the jet geometry and flow parameters on surface thermal uncertainty. As a consequence, the parameters impact on the mean surface heating under perturbations are found similar to that in baseline freestream condition. Moreover, only jet entry diameter and total-pressure ratio of jet-to-freestream are important when it comes to the standard deviation of surface heating. This research is anticipated to be available of robust thermal-reduction optimization on hypersonic vehicles with blunt-shape head in a wide range of free incoming conditions for reference.

1. Introduction

On account of severe aero heating on nose, growing interests have been drawn on the thermal protection system (TPS) [1] of hypersonic vehicles recently. Forward-facing cavities [2,3], counterflowing jets [4–6], aerospikes [7–9], and their combining schemes [10–13] are the main approaches utilized in TPS of hypersonic vehicles. In the review papers [14,15], Huang has summarized the outstanding performances of the counterflowing jet and its combinations, and the aerospike and its combinations on drag and heat flux reduction. Sun [16] has organized the literatures that using the numerical simulations to research on the drag and heat reduction configurations, and summarized them into a table. Wang has done a similar work [17], but his focus is the experimental investigations. And the readers could refer to their papers for more information. Preceding research [18] reveals that reverse jets positioned at the stagnation zone of the body can provide efficient surface thermal reduction. In that case, attentions are focused on the counterflowing jet schemes in this paper.

Previous researches [4,19] show that there exist two motion modes in flow structures of the blunt body with antidromic injection, including the long penetration mode (LPM) and the short penetration mode (SPM). The two motion modes are separated by a critical point of jet-to-freestream total-pressure ratio (*PR*), which is defined in Eq. (1). p_{oj} and $p_{o\infty}$ in Eq. (1) are the total pressure of the jet flow and the freestream flow, respectively.

$$PR = \frac{p_{oj}}{p_{o\infty}} \tag{1}$$

The flow structure becomes LPM when *PR* is lower than the critical value, and SPM when *PR* is larger than that. The two motion modes are displayed in Fig. 1. In the left side, the unstable multi-cell jet structure in LPM mode appears with oscillation motions, thus painful aero-heating effects thus occur owing to wide variation, and surface heat flux even increases, which are difficult to simulate. In the right side, the flow is stable when it comes to SPM mode. The cooling gas from the jet develops a steady recirculating region, resulting in low and even negative surface heating,

* Corresponding author.
E-mail address: yanchao@buaa.edu.cn (C. Yan).

https://doi.org/10.1016/j.ast.2020.106260
1270-9638/

Nomenclature

Ma_∞	freestream Mach number
Ma_j	the unit jet Mach number
Re_∞	freestream Reynolds number
Re_c	cell Reynolds number
α	freestream angle of attack
ρ	density
p	pressure
p_{oj}	total pressure of the jet flow
$p_{o\infty}$	total pressure of the freestream flow
p_{of}	freestream Pitot pressure
PR	the jet-to-freestream total-pressure ratio
PR_f	the ratio of jet total pressure to the freestream Pitot pressure
T	temperature
T_w	wall temperature
T_{aw}	the adiabatic wall temperature
T_{oj}	jet entry total-temperature
γ	the specific heat ratio, 1.4.
u_i	the ith velocity component
τ_{ij}	shear stress tensor
μ	coefficient of dynamic viscosity
δ_{ij}	Kronecker delta function
E	the total energy
H	the total enthalpy
q_j	heat flux
q_w	heat flux on surface
η	coefficient of thermal conductivity
k	turbulent kinetic energy
ω	specific dissipation rate of turbulence
μ_L	the laminar viscosity
μ_T	the turbulent viscosity
Ω	the vorticity magnitude
St	the Stanton number
S	the sum of squares in analysis of variance method
S_A	the sum of squares of factor A in analysis of variance method
S_E	the sum of squared errors in analysis of variance method
df	the freedom degree of each factor in analysis of variance method
MS	the mean square of each factor in analysis of variance method
F	the statistic describing factor significance in analysis of variance method
$Sig.$	the statistical significance of each factor in analysis of variance method
P	percentage form influence of each factor in analysis of variance method
ξ	random variable in polynomial chaos
$f(\xi)$	the probability density function of the random variable
$w(\xi)$	the orthogonal weight function of the random variable
d_m	the model diameter, 50 mm
D	the entry diameter of the nozzle
L	the length of the nozzle
L/D	the ratio of the nozzle length to the entry diameter
δ	the half expansion angle of the nozzle
L_c	the length of the model cylindrical part
θ	the angle measured from model central axis

Subscript

j	jet
w	wall
∞	freestream

Abbreviations

TPS	thermal protection system
LPM	long penetration mode
SPM	short penetration mode
NS	Navier-Stokes equations
RANS	Reynolds-Averaging Navier-Stokes equations
SST	the shear stress transport turbulence model
CFD	computational fluid dynamics
ANOVA	analysis of variance method
PCE	polynomial chaos expansions
NIPC	non-intrusive polynomial chaos
LHD	Latin hypercube design
W.w.	Windward
L.w.	Leeward

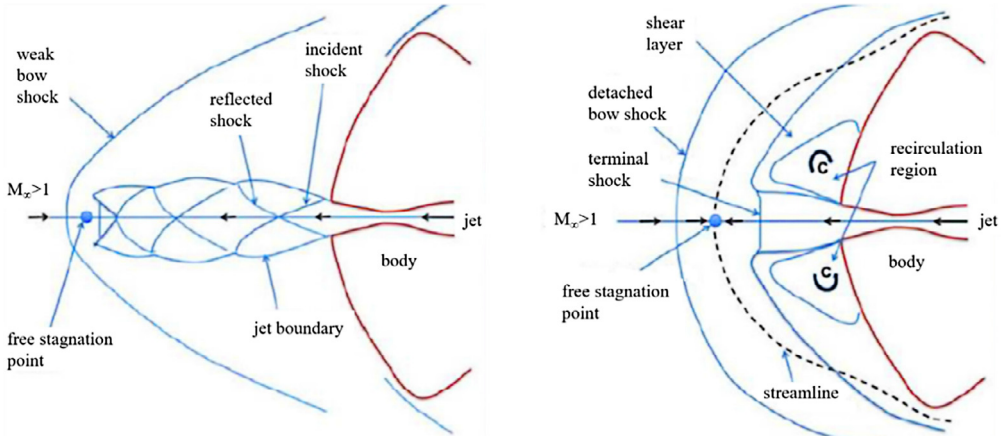

Fig. 1. Flow structure diagram for a) LPM, and b) SPM [20].

hence producing an effective thermal-reducing effect. Therefore, only stabilized blunt body flows under short penetration mode are researched in current paper.

Meyer [21] investigated the impacts of supersonic opposing jet flow on a blunt body under hypersonic mainstream condition, and found that the opposing jet has certain effects on the drag and

surface aero-thermal reduction. Hayashi [22] found in his experiments that significant reduction of surface aerodynamic heating on blunt body under stable condition can be obtained when opposing jet is added, while no reduction can be achieved under unsteady condition. He also conducted numerical simulations [23] and indicated that jet conditions greatly affect the performance of the thermal protection system with opposing jets. In the high enthalpy flow wind tunnel experiments [24] carried by Takashige, nitrogen and helium were injected out of the opposing jet nozzle, and were found to be capable of reducing the heat transfer on surface with effect. To realize the thermal protection of vehicles, Li studied the reverse jet technology in his master's thesis [25]. He also simulated the drag reduction effect under a non-zero angle of attack, and proposed a scheme of combined jets. The influence of a forward-facing micro-jets array was explored in Refs. [26,27]. It was revealed that the jets array performs well in surface heating reduction. Up to nearly 40% of surface heating reduction can be achieved even when *PR* is low. Guo [28] investigated the impacts of the jet flow parameters and the free incoming flow parameters on surface heat flux in her paper. It is indicated that *PR* is the most influential factor, followed by the incoming Mach number. However, she only focused on which factors would be important on a single-and-determinate baseline state essentially, rather than those states disturbed. This kind of research can provide useful information for determinate optimization of similar shape vehicles, while may not be that well for robust optimization, however.

When perturbations exist in the free incoming condition, surface heating will be varied, and uncertainty is bound to occur. Will the opposing jet flow, well designed for determinate free incoming condition, still be well for surface thermal reduction under perturbations? In current paper, the jet geometry and flow parameters will be set as the jet design parameters. Effects of these parameters will be investigated on surface heating uncertainty caused by free incoming perturbations. Instructive information can be provided for robust optimization of opposing jets.

In this paper, two-layers research structure is designed for analyzing the jet parameters influence on surface thermal uncertainty. The non-intrusive polynomial chaos method (NIPC) [29,30] is employed in the inner layer to quantify the surface thermal uncertainty of the blunt body caused by perturbations on free incoming Mach number Ma_∞ and angle of attack α. The analysis of variance method (ANOVA) is utilized in the outer layer to study the influence of the jet geometry and flow parameters on surface thermal uncertainty quantified from the inner layer. Previous to this, ANOVA is utilized to investigate the jet parameters influence on surface heating under different free incoming conditions, to reveal the variation of parameters influence, and to uncover the importance of studying parameters influence on surface thermal uncertainty.

The remainder of current paper is structured as follows. Section 2 depicts the basic principles of computational fluid dynamics algorithm for obtaining aerodynamic heating on surface. Methodologies of outer-layer ANOVA parameters study and inner-layer NIPC uncertainty quantification are briefly outlined in Section 3 and 4 respectively. Section 5 gives a generalization of the research problem, and verifies the independence of grids. Section 6 is the main research part of this paper. In this section, the baseline case will be studied. And the reversed-jet parameters influence will be analyzed on surface heating at several different free incoming conditions. Moreover, these parameters will then be researched on surface heating uncertainty under free incoming perturbations. Eventually, the paper is concluded in Section 7.

2. Numerical method

The main algorithms for calculating the surface aero-heating are refined as below.

2.1. Governing equations

Written in conservation law, the governing Navier-Stokes (NS) equations [31] are in the form of:

$$\frac{\partial \rho}{\partial t} + \frac{\partial (\rho u_i)}{\partial x_i} = 0 \tag{2}$$

$$\frac{\partial}{\partial t}(\rho u_i) + \frac{\partial}{\partial x_j}\left(\rho u_j u_i\right) = -\frac{\partial p}{\partial x_i} + \frac{\partial \tau_{ij}}{\partial x_j} \tag{3}$$

$$\frac{\partial}{\partial t}(\rho E) + \frac{\partial}{\partial x_j}\left(\rho u_j H\right) = \frac{\partial}{\partial x_j}\left(u_i \tau_{ij} - q_j\right) \tag{4}$$

with ρ the density, u_i the ith velocity component, and τ_{ij} the tensor of shear stress defined in:

$$\tau_{ij} = \mu\left(\frac{\partial u_i}{\partial x_j} + \frac{\partial u_j}{\partial x_i}\right) - \frac{2}{3}\mu\frac{\partial u_k}{\partial x_k}\delta_{ij} \tag{5}$$

Herein μ and δ_{ij} are respectively the coefficient of dynamic viscosity and the Kronecker delta function. The pressure p is acquired from the state equation for perfect gas as in Eq. (6), with T the temperature and γ the specific heat ratio 1.4. Besides, k in Eq. (6) is the turbulent kinetic energy simulated in the next Subsection.

$$p = \rho RT = (\gamma - 1)\left[\rho E - \rho k - \frac{1}{2}\rho\left(u^2 + v^2 + w^2\right)\right] \tag{6}$$

E and H are severally the total energy and total enthalpy evaluated in Eq. (7), with e and h denoting the internal energy and enthalpy.

$$\begin{aligned} E &= e + k + \frac{1}{2}\left(u^2 + v^2 + w^2\right) \\ H &= h + k + \frac{1}{2}\left(u^2 + v^2 + w^2\right) \\ h &= e + \frac{p}{\rho} \end{aligned} \tag{7}$$

The heat flux is obtained from Eq. (8), where η is the coefficient of thermal conductivity.

$$q_j = -\eta\frac{\partial T}{\partial x_j} \tag{8}$$

2.2. Turbulence model

For the sake of description for turbulent fluctuations, Reynolds-Averaging will be used in compressible N-S equations [31]. In order to close the Reynolds-Averaging Navier-Stokes equations, the k-ω shear stress transport (SST) model [32] developed by Menter is coupled into the equations with compressible correction [33], which has been applied in existing research [34–37] on reverse jet configurations. Another widely used turbulence model in aerodynamic simulations, the Spalart-Allmaras (SA) model [38], is also considered into comparison in Subsection 2.4 for validation of the influence of the turbulence models on predicted results. Consisting two transport equations of turbulent kinetic energy k and the specific dissipation rate of turbulence ω, the SST model is described as below.

$$\begin{aligned} \frac{\partial (\rho k)}{\partial t} + \frac{\partial \left(\rho u_j k\right)}{\partial x_j} &= \frac{\partial}{\partial x_j}\left[\left(\mu_L + \frac{\mu_T}{\sigma_k}\right)\frac{\partial k}{\partial x_j}\right] \\ &\quad + P_k - \beta^* \rho\omega k \end{aligned} \tag{9}$$

$$\frac{\partial(\rho\omega)}{\partial t}+\frac{\partial\left(\rho u_j\omega\right)}{\partial x_j}=\frac{\partial}{\partial x_j}\left[\left(\mu_L+\sigma_\omega\mu_T\right)\frac{\partial\omega}{\partial x_j}\right]+P_\omega-\beta\rho\omega^2 +2\left(1-f_1\right)\frac{\rho\sigma_{\omega2}}{\omega}\frac{\partial k}{\partial x_j}\frac{\partial\omega}{\partial x_j} \quad (10)$$

herein μ_L is the laminar viscosity. The turbulent viscosity μ_T is defined as:

$$\mu_T=\frac{a_1\rho K}{\max\left(a_1\omega,\, f_2\left\|\Omega\right\|\right)}$$

with Ω the vorticity magnitude. P_k and P_ω are the production terms of k and ω, acquired from:

$$P_k=\mu_T\Omega^2,\quad P_\omega=C_\omega\rho\Omega^2$$

In SST model, the standard k-ε model is applied in free shear layers and the outer region as well as the original k-ω model in the boundary layer near solid wall. Consequently, two sets of constants utilized above, are obtained from:

$$\phi=f_1\phi_1+\left(1-f_1\right)\phi_2,\quad f_1=\tanh\left(\Gamma_1^4\right)$$

$$\Gamma_1=\min\left[\max\left(\frac{\sqrt{K}}{0.09\omega d},\frac{500\mu_L}{\rho\omega d^2}\right),\frac{4\rho\sigma_{\omega2}K}{CD_{K\omega}d^2}\right]$$

$$CD_{K\omega}=\max\left(2\frac{\rho\sigma_{\omega2}}{\omega}\frac{\partial K}{\partial x_j}\frac{\partial\omega}{\partial x_j},1\times10^{-20}\right)$$

with d the distance from the nearest wall. f_2 is evaluated as:

$$f_2=\tanh\left(\Gamma_2^4\right),\quad \Gamma_2=\max\left(\frac{2\sqrt{K}}{0.09\omega d},\frac{500\mu_L}{\rho\omega d^2}\right)$$

The constants $K=0.41$, $a_1=0.31$, and the constant coefficients of these two sets are

$$\sigma_{k1}=0.85,\quad \sigma_{\omega1}=0.5,\quad \beta_1=0.075,\quad C_{\omega1}=0.533$$

$$\sigma_{k2}=1.0,\quad \sigma_{\omega2}=0.856,\quad \beta_2=0.0828,\quad C_{\omega2}=0.440$$

2.3. Discretization and boundary conditions

Discretization of the equations above is performed on the multi-block structured mesh on appliance of the finite volume approach [39]. The inviscid fluxes are discretized by employing the Roe flux-difference procedure, along with the second-order MUSCL reconstruction and the minmod limiter. Implicit LUSGS scheme is utilized for time integration.

The solid wall surface condition is specified as isothermal, with normal zero-gradient for pressure and non-slip for velocity on the wall. The symmetry plane condition is settled at the velocity, whose component normal to the plane is zero. Assigned at the opposing jet nozzle entry, the jet condition consists of the ratio of the jet-to-freestream total-pressure (PR), the jet entry total-temperature (T_{oj}), and the unit jet Mach number (Ma_j). The remaining boundaries are set as far-field specified with static pressure, static temperature, and Mach number. In addition, the freestream values of k, ω and μ_T in SST model at far-field are stipulated as [32,39]:

$$\frac{k_\infty}{a_\infty^2}=9\times10^{-9},\quad \frac{\omega_\infty}{\left(\rho_\infty a_\infty^2\right)/\mu_{L,\infty}}=1\times10^{-6},$$

$$\frac{\mu_{T,\infty}}{\mu_{L,\infty}}=0.009$$

The levels of k and ω at the wall are respectively specified as:

$$k_{wall}=0,\quad \omega_{wall}=\frac{60\mu_L}{0.075\rho\left(d_1\right)^2}$$

herein, d_1 is defined as the distance to the solid wall from the nearing first grids cell centers.

Table 1
Flow conditions for verification.

Verification flow conditions			Value
Freestream	Mach number	Ma_∞	3.98
	Angle of attack (deg.)	α	0
	Total pressure (MPa)	$P_{o\infty}$	1.37
	Total temperature (K)	$T_{o\infty}$	397
Jet	Mach number	Ma_j	1
	Total temperature (K)	T_{oj}	300
	Total-pressure ratio of jet-to-freestream	PR	0.4, 0.6, 0.8
Wall temperature (K)		T_w	295

2.4. Code validation

Surface thermal predicting capabilities of the numerical method above on blunt bodies adding reversed jets are verified below. Two estimations of heat flux, including local methods and integral relationships, are compared in Refs. [40,41], and the local method will be utilized in current paper. The chemistry is important for surface heating estimation in hypersonic flows [42], however existing researches [7,13,18] on blunt-body thermal reduction are carried out without considering the chemistry, and can draw good conclusions. Thus, no chemistry will be considered in current paper for convenience.

Experiments performed by Hayashi [22] in 2006 are chosen as validation examples. The freestream and jet flow conditions are displayed in Table 1. Nitrogen is the jet species in Hayashi's experiments, which is replaced by air in this simulation. Due to the similarities between air and nitrogen in molecular weights, viscosity and thermophysical features, accordant flow fields and aerodynamic thermal peculiarities will be generated for the jet configuration [43]. Since the freestream Reynolds number Re_∞ is about 4.2×10^7/m high, the influence of turbulence should be considered. Previous works [44–46] have indicated that the influences of turbulence models cannot be neglected. This paper will evaluate the influences of turbulence models, including the SST model and the SA model, which are the most widely used in aerodynamic simulations.

The Stanton number St in Fig. 2 is utilized to describe the surface heat flux distributions. In definition of St in Eq. (11), q_w is the heat flux on surface, T_{aw} is the wall temperature which is adiabatic, and the Prandtl number Pr_w is 0.71. The simulated St distributions under different PRs via different turbulence models are compared with those from the experiments and the referenced CFD simulations of Guo [28], as shown in Fig. 2. It can be observed that, the SST simulations are more consistent and closer to the experimental data, compared to the SA results. At the same time, the St distribution, which is simulated from the SST turbulence model, ranges in the middle of the experimental data and the referenced CFD results. It is more identical with the experimental data compared from the referenced CFD results. Therefore, the SST model is selected to simulate the turbulence influences on predicted results in this paper.

$$St=\frac{q_w}{\left(T_{aw}-T_w\right)\rho_\infty Cp_\infty u_\infty};$$

$$T_{aw}=T_\infty\left[1+\sqrt[3]{\mathrm{Pr}_w}\left(\frac{\gamma-1}{2}\right)Ma_\infty^2\right] \quad (11)$$

Comparisons between the simulated density gradient contours and the Schlieren figures from experiments [22] under different PRs are exhibited in Fig. 3. Good agreements are formed between

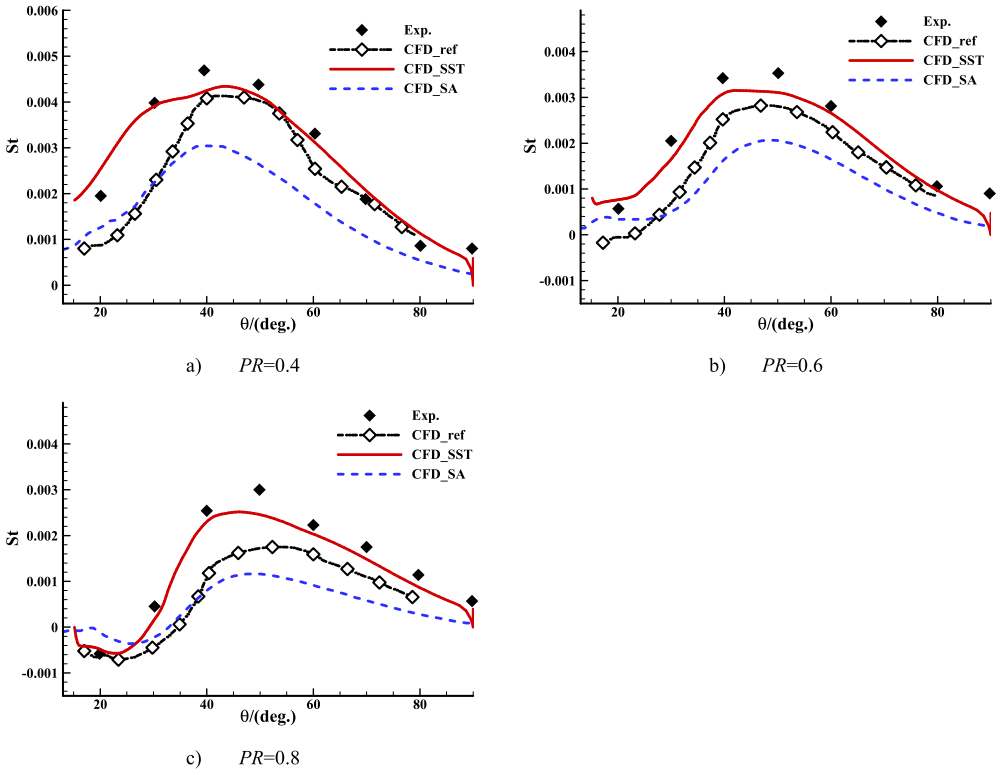

Fig. 2. Verification of aerodynamic thermal prediction.

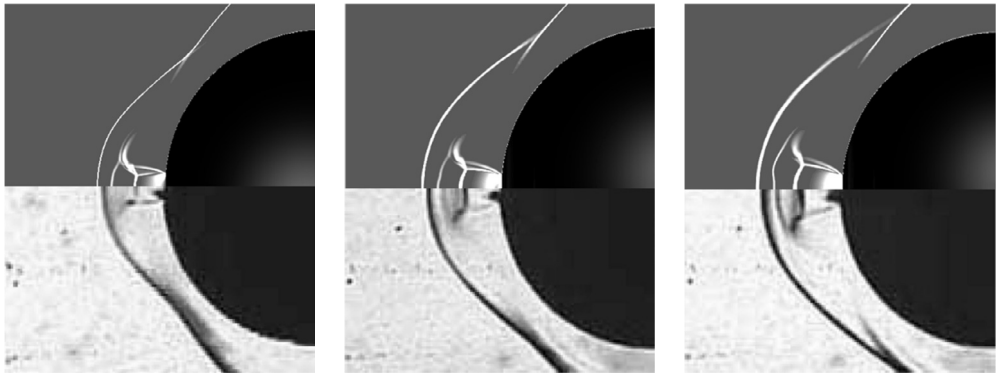

Fig. 3. Comparison between CFD simulation (Upper) and Schlieren results (Lower) under different *PR*s.

flow structures of the simulations and the experiments. Although the distances of the bow shock, the interface, and the Mach disk from surface in current simulations are respectively a little larger than those of the experiments, it could be caused from the replacement of air as the injection gas. Combined with comparisons in Fig. 2, the accuracy and reliability of the numerical method for aero thermal simulation of blunt body with reversed injections can be verified.

3. Methodology of parameters study

The Analysis of Variance (ANOVA) method, coupling with the orthogonal experimental design, will be applied to explore the parameters influence and significance on surface thermal property. The ANOVA approach is a statistical method utilized to distinguish the differences in experimental results due to changes in factor levels from those due to fluctuations in experimental errors [47]. This approach could be applied to investigate the influences of parameters on the selected target functions. Huang is an excellent expert on the data mining technique based on ANOVA, he and his team have done a lot of relative researches, including parametric analyses on the cavity flameholder [47,48], the single expansion ramp nozzle [49], the three-dimensional transverse jet [50], the combination configuration of an aerospike and an opposing jet [51], and the micro-ramp vortex generator within scramjet combustors [52], etc. They have deeply explored the information of these geometric configurations with the variance analysis approach, which provide useful information for optimization design. This approach has also been well performed by Ju to measure the parameters sensitivity of energy addition on scramjet nozzle properties [53].

Take A as a factor for instance. In order to measure the difference between the r levels of input factor A, the average results of each different level of A will be considered. ANOVA is performed

Table 2
Parameters definition of variance analysis method.

Source	S	df	MS	F	$Sig.$	$P/\%$
A	S_A	df_A	$MS_A = S_A/df_A$	$F_A = MS_A/MS_E$	$Sig_A.$	$P_A = S_A/S_T$
B	S_B	df_B	$MS_B = S_B/df_B$	$F_B = MS_B/MS_E$	$Sig_B.$	$P_B = S_B/S_T$
...	...	...	...	...	...	...
$Error$	S_E	df_E	$MS_E = S_E/df_E$			
$Total$	S_T	df_T				

based upon the decomposition of the sum of squares and the freedom degrees. Considering the statistics below [54],

$$S_T = \sum_{i=1}^{r}\sum_{j=1}^{n_i}\left(x_{ij} - \bar{x}\right)^2 \quad \bar{x} = \frac{1}{n}\sum_{i=1}^{r}\sum_{j=1}^{n_i} x_{ij} \tag{12}$$

where x_{ij} is the jth sample in the ith sub-population, in which case the input factor A is on the ith level; n_i is the number of the ith sub-population; $\bar{x}$ is the average of the whole population; n is the number of the whole population; S_T is the total sum of squares, which can be broken down in Eqs. (13)–(14).

$$S_T = S_E + S_A \tag{13}$$

$$\begin{cases} S_E = \sum_{i=1}^{r}\sum_{j=1}^{n_i}\left(x_{ij} - \bar{x}_{i\cdot}\right)^2 \\ S_A = \sum_{i=1}^{r}\sum_{j=1}^{n_i}\left(\bar{x}_{i\cdot} - \bar{x}\right)^2 \end{cases} \tag{14}$$

Herein, $\bar{x}_i$ is the average of the ith sub-population; S_E is the sum of squared errors, which represents the effect of experimental random error and unconsidered factors interaction; S_A is the sum of squares of input factor A, on behalf of the effect of A in the total variation.

Parameters definition of ANOVA method thus can be listed in Table 2. 'S' and 'df' are respectively the sum of squares and freedom degree of the factor. 'MS' is the mean square described as the ratio of the sum of squares to the freedom degree of the factor. Defined as the mean square ratio of the factor to the error term, 'F' is the statistic describing the factor significance by comparing with the statistical error. '$Sig.$' is the statistical significance of the input factor calculated from 'F' of the input factor and 'df's of the input factor and the error term. Separated by 0.05 and 0.01, the value of '$Sig.$' represents that the input factor is 'not significant', 'significant', and 'extremely significant' respectively. The factor will be more significant when '$Sig.$' is smaller and closer to 0. 'P' in percentage form is the ratio of each factor's squares sum to that of the whole, which represents the contribution of the factor to the whole. The factor is more influential when 'P' of that is bigger.

4. Methodology of uncertainty quantification

In order to measure the uncertainty characteristics under free incoming perturbations, the point-collocation NIPC method [55] is performed on samples obtained from Latin hypercube sampling design (LHD) [56] to create a stochastic polynomial model between the CFD outputs (i.e. surface heat flux) and the disturbance sources.

The key issue is to determine the coefficients of the polynomial chaos expansions (PCE). With the PCE approach, a response function Y^* could be projected to orthogonal basis functions:

$$Y^*(x,\xi) \approx \sum_{i=0}^{P} a_i(x)\psi_i(\xi) \tag{15}$$

where Y^* is supposed to be a function of the n-dimensional standard random vector $\xi = (\xi_1, \ldots, \xi_n)$, as well as the deterministic vector x.

It is infinite theoretically for series of Eq. (15), whereas the PCE is truncated for implementation, which is a discrete sum of numerous orthogonal basis functions. The total number of samples N_s will be obtained from dimension of the standard random vector n, the oversampling ratio n_D, which is recommended as 2 in Ref. [57], along with the truncated order of the polynomial chaos expansion D. The specific relation is defined in Eq. (16):

$$N_s = n_D \cdot (P+1) = n_D \cdot \left[\frac{(n+D)!}{n!D!}\right] \tag{16}$$

The deterministic CFD simulations are applied in this research to acquire the stochastic response function Y^*. The least quadratic regression method is then utilized for solving the linear equations.

$$\begin{pmatrix} Y^*(x,\xi_0) \\ Y^*(x,\xi_1) \\ \cdots \\ Y^*(x,\xi_{N_s-1}) \end{pmatrix} = \begin{pmatrix} \psi_0(\xi_0) & \psi_1(\xi_0) & \cdots & \psi_P(\xi_0) \\ \psi_0(\xi_1) & \psi_1(\xi_1) & \cdots & \psi_P(\xi_1) \\ \cdots & \cdots & & \cdots \\ \psi_0(\xi_{N_s-1}) & \psi_1(\xi_{N_s-1}) & \cdots & \psi_P(\xi_{N_s-1}) \end{pmatrix} \begin{pmatrix} a_0 \\ a_1 \\ \cdots \\ a_P \end{pmatrix} \tag{17}$$

The mean value μ_{Y*} and standard deviation σ_{Y*} of response Y^* can be achieved in Eqs. (18)–(20).

$$\begin{aligned} \mu_{Y*} &= E\left[Y^*(\xi)\right] = \int Y^*(\xi) f(\xi) d\xi \\ &= \int \sum_{i=0}^{P} a_i \psi_i(\xi) f(\xi) d\xi \\ &= a_0 \int \psi_0(\xi) f(\xi) d\xi + \sum_{i=1}^{P} a_i \int \psi_i(\xi) f(\xi) d\xi \\ &= a_0 + \sum_{i=1}^{P} a_i \frac{f}{w} \int \psi_0 \psi_i w d\xi \\ &= a_0 \end{aligned} \tag{18}$$

$$\begin{aligned} \sigma^2_{Y*} &= D\left[Y^*(\xi)\right] = E\left[\left(Y^*(\xi) - a_0\right)^2\right] \\ &= \int \left[\sum_{i=1}^{P} a_i \psi_i(\xi)\right]^2 f(\xi) d\xi \\ &= \sum_{i=1}^{P}\sum_{j=1}^{P} a_i a_j \int \psi_i(\xi)\psi_j(\xi) f(\xi) d\xi \\ &= \sum_{i=1}^{P}\sum_{j=1}^{P} a_i a_j \frac{f}{w} \int \psi_i \psi_j w d\xi \end{aligned}$$

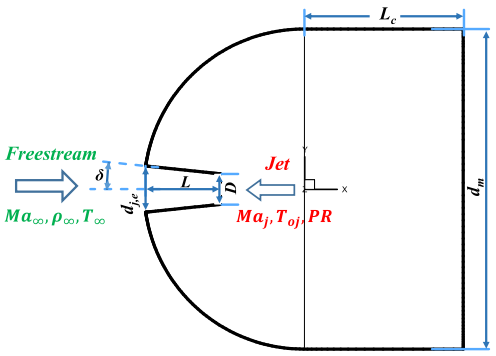

Fig. 4. Baseline geometry.

$$= \sum_{i=1}^{P} \left[a_i^2 \frac{f}{w} \left\langle \psi_i^2 \right\rangle \right] \tag{19}$$

$$\sigma_{Y*} = \sqrt{\sum_{i=1}^{P} \left[a_i^2 \frac{f}{w} \left\langle \psi_i^2 \right\rangle \right]} \tag{20}$$

Herein, $f(\xi)$ and $w(\xi)$ are the probability density function and the orthogonal weight function of the random variable ξ respectively. The ratio of f to w depends on distribution of the random variable:

$$\frac{f}{w} = \begin{cases} 1/\sqrt{2\pi}, & \text{when } \xi \text{ satisfies Normal distribution} \\ 1/2, & \text{when } \xi \text{ satisfies Uniform distribution} \end{cases} \tag{21}$$

5. Problem description

The problem researched in current paper will be prescribed in this section, including baseline geometry and flow conditions, jet design factors, and validation of mesh independency.

5.1. Baseline conditions

To denote the general hypersonic vehicle blunt-shape head, the baseline geometry model consists of a hemispheric forebody and a cylindroid main body, as displayed in Fig. 4. It is a three-dimensional model. A reverse nozzle jet is positioned at the stagnation point of the hemispheric forebody. The model diameter is $d_m = 50$ mm, the diameter of the reversed divergent nozzle entry is $D = 4$ mm, the nozzle length is $L = 8$ mm, the half expansion angle of the nozzle is $\delta = 0°$, and the cylindrical part length is $L_c = 0.5 d_m$. The coordinate origin is set at the hemisphere center.

Summarized in Table 3, the baseline flow condition is designed at an altitude of 30 km with zero angle of attack. Air is assigned as the jet coolant released from the entrance of the divergent nozzle positioned at the nose tip against hypersonic freestream. Allowing for the freestream unit Reynolds number about 2.26×10^6/m high, the turbulent effects are rationally considered in CFD simulations. The parameters study will be employed based on the baseline conditions above.

The inner-layer uncertainty quantification will be performed on the baseline freestream condition with perturbations, the outer-layer parameters study will be performed in the design space expanded from the baseline jet flow and geometry condition.

5.2. Jet design factors

For the parametric research, five design factors of the jet nozzle are investigated, including the nozzle entry diameter D, the nozzle length to the entry diameter ratio L/D, the nozzle half expansion angle δ, the jet total temperature T_{oj}, and the ratio of jet-to-freestream total-pressure PR. The variation range of these factors is summarized in Table 4.

Table 3
Baseline flow conditions.

Baseline flow conditions			Baseline level
Freestream	Mach number	Ma_∞	6
	Angle of attack (deg.)	α	0
	Density (kg/m^3)	ρ_∞	0.0184
	Temperature (K)	T_∞	226.5
Jet	Mach number	Ma_j	1
	Total temperature (K)	T_{oj}	300
	Total-pressure ratio of jet-to-freestream	PR	0.2
Wall temperature (K)		T_w	295

Since only expanding nozzles are researched here, rather than convergent ones, δ is assumed to vary from 0° to 6°. Other four parameters input all vary within ±20% of the baseline level respectively.

Furthermore, as another considerable controlling factor defined in Eq. (22), the total pressure ratio PR_f is underlined for governing the mode to be unsteady LPM or steady SPM [4]. When PR_f exceeds the critical value, the flow motion mode is steady SPM.

$$PR_f = p_{oj}/p_{of} \tag{22}$$

Here p_{of} is the freestream Pitot pressure, namely the total pressure behind the normal shock. On basis of the normal shock formula and the isentropic stagnation assumption, the p_{of} can be estimated from the Rayleigh Pitot tube relation [58]:

$$p_{of} = p_\infty \left(\frac{(\gamma+1)^2 Ma_\infty^2}{4\gamma Ma_\infty^2 - 2(\gamma-1)} \right)^{\frac{\gamma}{\gamma-1}} \frac{1-\gamma+2\gamma Ma_\infty^2}{\gamma+1} \tag{23}$$

The jet total pressure p_{oj} can be approximated from the PR definition as well as the isentropic flow relation [58],

$$\begin{aligned} p_{oj} &= PR \cdot p_{o\infty} \\ p_{o\infty} &= p_\infty \left(1 + \frac{\gamma-1}{2} Ma_\infty^2 \right)^{\frac{\gamma}{\gamma-1}} \end{aligned} \tag{24}$$

As a summary of Eqs. (22)–(24), PR_f can be described as

$$PR_f = PR \cdot f\,(Ma_\infty) \tag{25}$$

in which, PR_f is positively related to PR. When Ma_∞ lies in the disturbance interval of $[5.4, 6.6]$ specified in Table 9 of Section 6, the $f(Ma_\infty)$ in Eq. (25) is an increasing function of Ma_∞. Therefore, the values of PR_f are located in $[3.509, 12.116]$ for all the simulations in this paper.

The critical value $PR_{f,crit}$ could be derived from a linear relation with the ratio of the body diameter D_e in the light of Finley's experimental findings [4].

$$PR_{f,crit} \propto D_e; \quad D_e = d_m/d_{j,e} \tag{26}$$

where $d_{j,e}$ is the nozzle exit diameter as shown in Fig. 4. According to Eq. (26), the critical total-pressure ratio $PR_{f,crit}$ will enlarge as the body diameter ratio D_e increases. Considering the nozzle geometry parameters' variation, the maximum D_e is 15.625, therefore the $PR_{f,crit}$ is estimated as 2.93. In this case, the criterion in Eq. (27) can be met, indicating that the steady SPM mode has been established in all the cases of current research.

$$PR_f > PR_{f,crit} \tag{27}$$

Table 4
Input factors variation range.

Factors		Varied range	Baseline	Lower bound	Upper bound
Nozzle entry diameter (mm)	D	±20%	4.0	3.2	4.8
Nozzle length-to-entry-diameter ratio	L/D	±20%	2.0	1.6	2.4
Nozzle half expansion angle (deg.)	δ	0^{+6}_{+0}	0	0	6
Jet total temperature (K)	T_{oj}	±20%	300	240	360
Total-pressure ratio of jet-to-freestream	PR	±20%	0.2	0.16	0.24

Table 5
Experimental design for jet parameters.

Test number	PR	T_{oj}/K	D/mm	L/D	δ/(deg.)
1	0.16	240	3.2	1.6	0
2	0.16	300	4.0	2.0	3
3	0.16	360	4.8	2.4	6
4	0.20	240	3.2	2.0	3
5	0.20	300	4.0	2.4	6
6	0.20	360	4.8	1.6	0
7	0.24	240	4.0	1.6	6
8	0.24	300	4.8	2.0	0
9	0.24	360	3.2	2.4	3
10	0.16	240	4.8	2.4	3
11	0.16	300	3.2	1.6	6
12	0.16	360	4.0	2.0	0
13	0.20	240	4.0	2.4	0
14	0.20	300	4.8	1.6	3
15	0.20	360	3.2	2.0	6
16	0.24	240	4.8	2.0	6
17	0.24	300	3.2	2.4	0
18	0.24	360	4.0	1.6	3

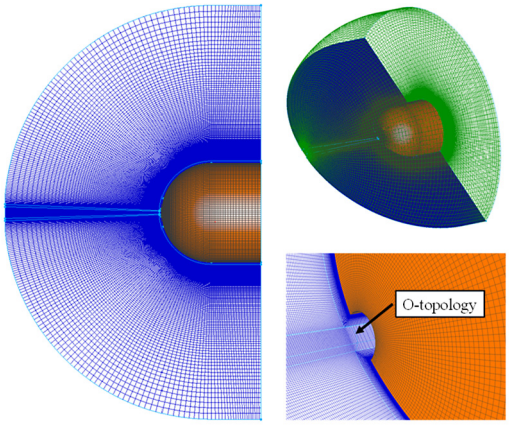

Fig. 5. Grid topology.

Thereafter, an orthogonal sample set of eighteen samples is generated for jet design parameters. Each input jet parameter has three levels (i.e. $PR\epsilon${0.16, 0.20, 0.24}, $T_{oj}\epsilon$\{240, 300, 360\}, $D\epsilon$\{3.2, 4.0, 4.8\}, $L/D\epsilon$\{1.6, 2.0, 2.4\}, $\delta\epsilon$\{0,3,6\}), with the experimental arrangement shown in Table 5.

5.3. Grid independence verification

As demonstrated in Fig. 5, o-topology grids are partitioned to achieve accurate simulations for the complicated flow-fields of freestream-jet-coupling configuration. For the sake of accurate imitation of the surface heating, the cell Reynolds number Re_c defined in Eq. (28), is fixed to no more than ten to strictly control the first grid height [59]. Δx_n is the first grid layer normal height near the solid wall.

$$Re_c = \frac{\rho_\infty u_\infty \Delta x_n}{\mu_\infty} \tag{28}$$

Moreover, three scales of grids, including coarse, medium, and fine grids with detailed information shown in Table 6, are utilized to verify the grid independence under the baseline flow condition. Prior to this, it should be considered that accumulation of errors occurs at each integration step, and is necessary to be evaluated in CFD simulations [60,61]. The accumulation errors of these three grids are estimated in Table 7. It can be drawn that the accumulation error is allowed, since the integration steps ratio of the maximum allowable to the actual (R_s) is greater than 1 for each grid.

Table 6
Grid information.

Grids	Coarse	Medium	Fine
First cell height (mm)	0.006	0.004	0.002
Re_c	13.56	9.04	4.52
Cell number	1525500	2464000	4142500

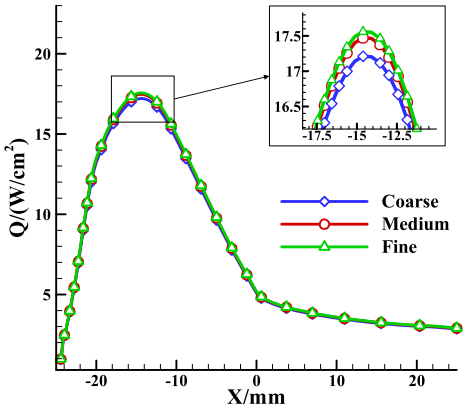

Fig. 6. Comparison of surface heat flux between different grid scales.

After the estimation of accumulation errors, comparisons of surface heat flux and pressure distributions are respectively made between these grids, as Fig. 6 and Fig. 7 display. Results reveal that surface heat flux distributions of these grids have only slightly difference, and the pressure does the same. Consequently, the medium grid scale is elaborate enough and will be applied in subsequent study to ensure the numerical accuracy, as well as saving computing resources.

6. Results and discussion

6.1. Baseline results

Ahead of implementing the uncertainty quantification and the jet parameters study, the flow field around baseline geometry model in Fig. 4 under baseline flow condition in Table 3 will be revealed. The three-dimensional simulation is performed in the

Table 7
Estimations of accumulation errors of three grid scales.

Grids		S_1	S_2	S_3	S_{err}	S^{max}	n	n_{max}	R_s
Coarse	block1	2.90E-07	7.31E-07	4.41E-06	5.43E-06	0.05	30000	8.49E+07	2829.12
	block2	1.44E-07	3.36E-05	2.44E-04	2.78E-04	0.05	30000	3.24E+04	1.08
	block3	2.90E-07	7.54E-06	4.41E-06	1.22E-05	0.05	30000	1.67E+07	556.72
Medium	block1	2.40E-07	5.64E-07	1.88E-06	2.69E-06	0.05	30000	3.47E+08	11552.64
	block2	1.23E-07	1.45E-05	1.08E-04	1.23E-04	0.05	30000	1.66E+05	5.54
	block3	2.40E-07	4.41E-06	1.88E-06	6.53E-06	0.05	30000	5.87E+07	1956.13
Fine	block1	2.00E-07	2.90E-07	9.71E-07	1.46E-06	0.05	30000	1.17E+09	39039.15
	block2	1.06E-07	7.54E-06	5.69E-05	6.45E-05	0.05	30000	6.00E+05	20.01
	block3	1.44E-07	2.79E-06	9.71E-07	3.91E-06	0.05	30000	1.64E+08	5456.17

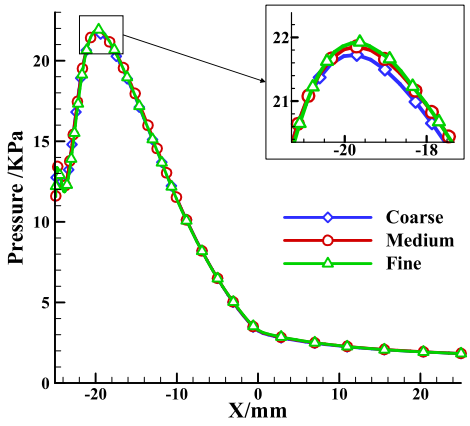

Fig. 7. Comparison of surface pressure between different grid scales.

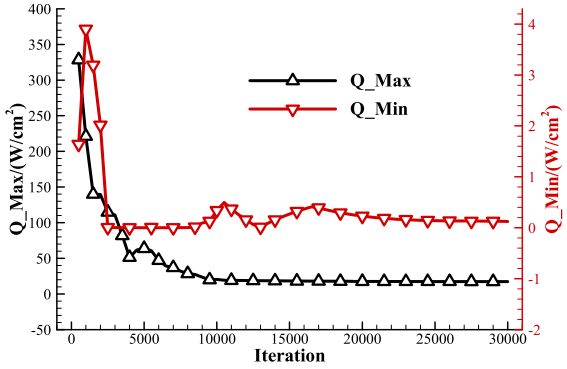

Fig. 8. Convergence history of the maximum and minimum of surface heat flux.

whole domain to obtain the flow field structure, which is applied in all the CFD simulations of this paper. The aerodynamic thermal reduction due to reversed jets will be investigated and compared to the no-jet results under baseline freestream condition.

Firstly, the iterative process of the maximum and minimum of the heat flux on surface of the baseline model is monitored, and the convergence histories are viewed in Fig. 8. It can be drawn that the simulations of the surface heat flux have converged. After the convergence validation, the flow field structure will be analyzed in detail.

The baseline shock-jet-interactive flow field is demonstrated in Fig. 9, with density-gradient contour and Mach number contour severally in the upper and lower side. Fig. 10 compares the temperature contour of the flow field with and without the nozzle jet. A complicated flow structure composed of multi shock waves and free shear layers is established caused by injection. The stand-off distance of shock-to-surface along stagnation line is 3.65 mm long in no-jet case; while it is 13.82 mm long (almost 3.8 times as long

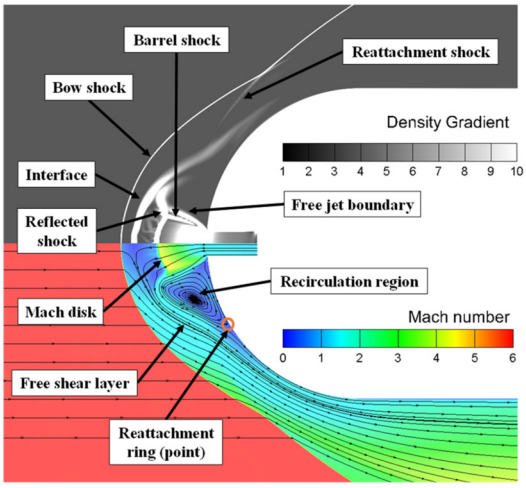

Fig. 9. Baseline flow field with reversed jet. (For interpretation of the colors in the figure(s), the reader is referred to the web version of this article.)

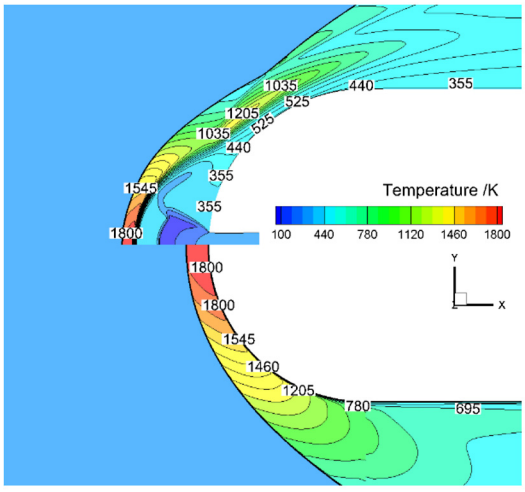

Fig. 10. Comparison of temperature distribution with (upper) and without (lower) jet.

as that in no-jet case) when the nozzle jet appears. Fig. 9 indicates that a conical free shear layer comes into being, when the jet flow comes back to the surface, after meeting mainstream at the interface. A low-temperature recirculation region then is generated. The reattachment shock emerges when the shear layer impinging the body surface, causing the temperature rise nearby the reattachment point. However, Fig. 10 illustrates that the high-temperature (over 1000 K) fluid is effectively separated from the body surface by the shear layer near the reattachment location. As a result of all, the high temperature region caused by the main shock is iso-

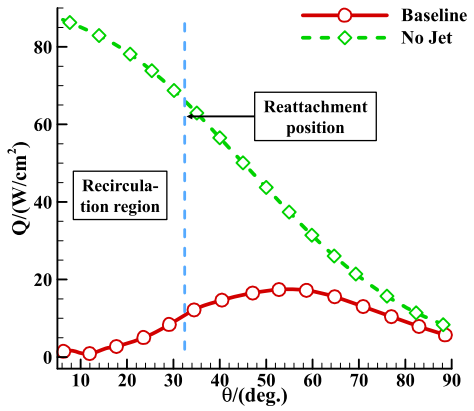

Fig. 11. Comparison of baseline surface heat flux on symmetry plane with and without injection.

lated from the body, and fluid around the body surface is much cooler compared to that without jets.

Baseline surface heat flux on symmetry plane with and without injection is compared in Fig. 11, with baseline reattachment position ($\theta = 32.44°$, θ is the angle measured from model central axis) also plotted. Compared to the no-jet case, the baseline surface heat flux is effectively decreased near the recirculation region, as a result of the low-temperature recirculation flow. On account of impingement of shear layer on surface and the heating effect after the reattachment shock, the temperature rises after recirculation region, and the surface heat flux rises consequently as exhibited in Fig. 10 and Fig. 11 respectively. The temperature and heat flux are reduced after the peak heat flux at a distance behind the reattachment position, on account of the flow expansion along the body surface.

Moreover, as integration of the surface heat flux, the total heat load on surface is another variable of interest. It is 832.98 W of total heat load in no-jet case, while 298.89 W in the baseline case with jets, demonstrating almost 64% of that reduced by jet. It is clear that the reversed jet at the nose tip can effectively reduce the heat transfer on surface.

6.2. Parametric study under different freestream conditions

Before investigating the jet parameters impact on surface thermal uncertainty under free incoming perturbations, comparisons are made between several different single-and-determinate freestream conditions to reveal the differences of the jet parameters influences on surface heating when free incoming conditions are varied.

The freestream conditions for comparison are set at three different points, including baseline condition $Ma = 6$, $\alpha = 0°$, Mach number varied condition $Ma = 5.5$, $\alpha = 0°$, and angle of attack varied condition $Ma = 6$, $\alpha = 6°$, with other free incoming parameters set as in Table 3. The $L_{18}(3^8)$ orthogonal experimental design in Table 5 will be arranged for the five jet design factors described in Table 4. In each of the three different free incoming conditions, CFD calculations will be carried out for each sample set in Table 5. ANOVA will then be developed at several surface gauging points, which are set the places where θ equals to 10°, 20°, ..., 90°. On that basis, comparisons will be drawn between these different freestream conditions.

6.2.1. Parameters study on surface heat flux

Parameters study will be firstly carried out on surface heat flux in this subsection, with surface total heat load analyzed in the next subsection.

1. Baseline $Ma = 6$, $\alpha = 0°$

Varying trend of the jet parameters sensitivity on surface heat flux under baseline freestream condition are illustrated in Fig. 12, with parameters influence in percentage and parameters significance in the left and right side respectively. By taking effect on the jet mass flow rate directly, the nozzle entry diameter D and the total-pressure ratio of jet-to-freestream PR are 'extremely significant' on surface heat flux. The impact of D is greater than 50% and even over 75% in some region. While it is less than 20% for PR. The next important factor is T_{oj}, which affects the surface heat flux by changing the jet flow temperature. T_{oj} is 'significant' and even 'extremely significant' when θ is greater than 50 degree. By changing the flow expansion inside the jet, the nozzle length-to-entry-diameter ratio L/D and the nozzle half expansion angle δ will affect the flow state at the jet exit, and finally take effect on the surface heat flux, which are almost 'not significant', however.

Nearby the jet exit at $\theta = 10°$, the parameters sensitivity is different from others. Ranked by importance on surface heat flux, the parameters are in order of D, T_{oj}, δ, PR, L/D at $\theta = 10°$, while it is D, PR, T_{oj}, L/D, δ at other θs. Due to the direct influence of the cooling jet flow, the effect of T_{oj} at $\theta = 10°$ is much more important and more significant than that at other gauging points. The half expansion angle δ has a direct effect on the expansion process at the nozzle exit, which indirectly affects the heat flux at $\theta = 10°$, and is 'extremely significant' in this case. The parameter L/D is 'not significant'.

2. Ma varies

In this part, comparisons of the jet parameters sensitivity are made between different Mach numbers, as demonstrated in Fig. 13. It can be observed that, when Mach number changes from 6 to 5.5, the overall significance of the parameters begins to weaken. Except for the increases of the influences of PR and L/D near the opposing nozzle exit at $\theta = 10°$, that of other factors are weakened. At other gauging points, the parameters D, T_{oj}, and PR are less significant than that of Mach 6, regardless of the parameters influence variation. δ becomes more important, whereas L/D is still of little importance, which are not displayed.

3. α varies

Parameters sensitivity on surface heat flux of the windward and leeward lines are researched when the freestream angle of attack is changed from 0° to 6°, which are compared with that in zero angle of attack, as pictured in Fig. 14 and Fig. 15 severally. 'W.w.' and 'L.w.' in the figures are the representations of windward and leeward.

With the emergence of angle of attack, the parameters influence on windward line is nearly unchanged, only the parameter significance decreases slightly. The effects of D and PR are further enhanced near the nozzle exit ($\theta = 10°$), while others weakened. At other gauging points, the influences of D, PR and T_{oj} do not change much, but the significances are reduced to some extent. δ and L/D are still 'not significant' factors, which are not shown in the figure.

Due to the angle of attack, flow structures at the leeward vary greatly along with the variation of the nozzle shape, resulting in irregular phenomena of parameters sensitivity on the leeward surface heat flux. The irregularity is particularly strong between the gauging points of 30° and 40° on account of the existence of the reattachment point and its position moving. The effect of D decreases by 20 to 30 percent, but it is still an 'extremely significant' factor. Besides, there is an increase of 15 to 25 percent of T_{oj},

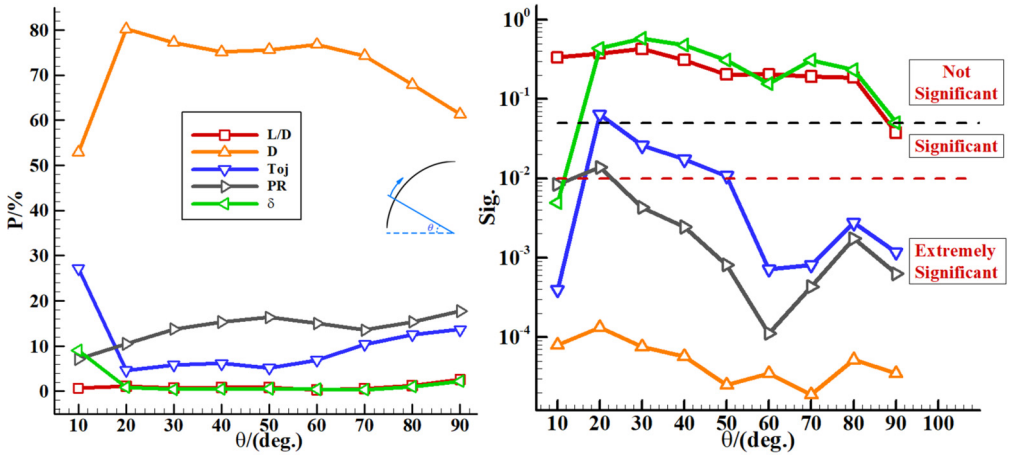

Fig. 12. Varying trend of jet parameters influence (Left) and significance (Right) along the blunt surface at baseline freestream condition.

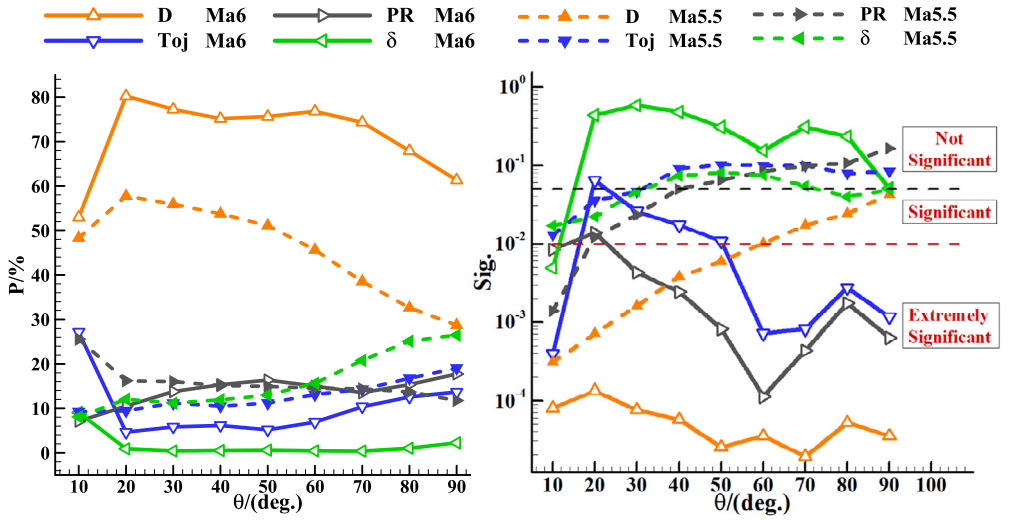

Fig. 13. Comparison of jet parameters influence (Left) and significance (Right) for Ma = 6 and Ma = 5.5.

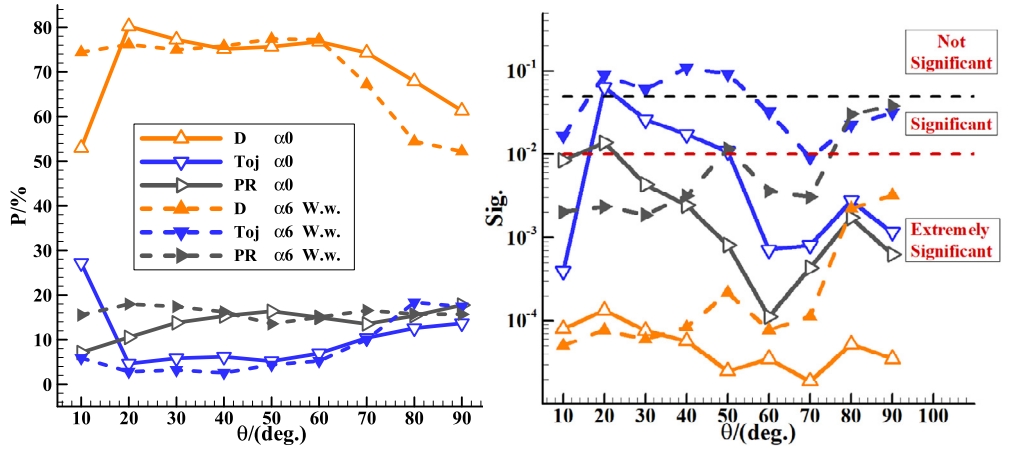

Fig. 14. Comparison of parameters sensitivity between $\alpha = 0°$ and $\alpha = 6°$ (Windward).

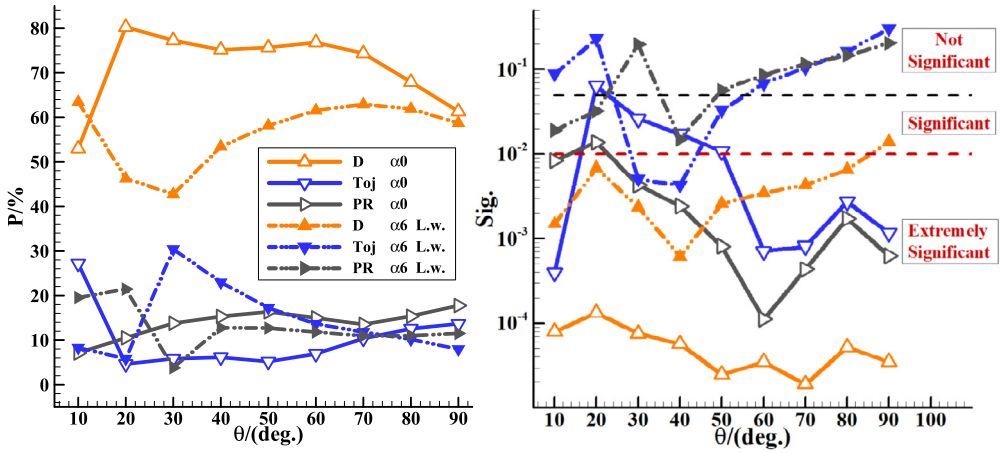

Fig. 15. Comparison of parameters sensitivity between $\alpha = 0°$ and $\alpha = 6°$ (Leeward).

Table 8
Parameters sensitivity on surface total heat load under different freestream conditions.

		L/D	D	T_{oj}	PR	δ
$P/\%$	$Ma6\alpha0°$	0.01	75.25	8.94	14.43	0.86
	$Ma6\alpha6°$	0.20	73.53	5.13	19.97	0.68
	$Ma5.5\alpha0°$	0.90	46.94	14.43	16.36	15.16
$Sig.$	$Ma6\alpha0°$	0.96109	0.00002	0.00071	0.00023	0.08731
	$Ma6\alpha6°$	0.42814	0.00002	0.00224	0.00009	0.11253
	$Ma5.5\alpha0°$	0.71439	0.00468	0.04979	0.03978	0.04556

whose significance also increases to an extreme degree. The influence of PR is slightly reduced about 2 to 10 percentage points, whose significance reduces to between 'not significant' and 'significant'. Though changed, the influences of the other two factors δ and L/D are still 'not significant', hence not displayed. At other measuring points, despite the effects of these parameters have increased or not, the significances all have decreased. Only D is an 'extremely significant' factor, with all the others almost 'not significant'.

6.2.2. Parameters study on surface total heat load

This subsection will explore the parameters sensitivity on surface total heat load under different freestream conditions, as demonstrated in Table 8. When the freestream angle of attack is varied from 0° to 6°, the jet parameters sensitivity on surface total thermal load does not change much. When the freestream Mach number diminishes from 6 to 5.5, the influence of T_{oj} and δ increases while D decreased. Furthermore, the overall significance of the jet parameters on surface total heat load declines.

6.3. Parametric study on surface heating uncertainty

On the basis of above, influences of the jet design parameters on surface heating have been changed obviously because of the variation of freestream Mach number and angle of attack. Consequently, when perturbations occurred in free incoming conditions, it is necessary to study the jet parameters influence on surface thermal uncertainty, to recognize which jet design parameters are important for robust optimization of blunt-shape vehicles. Perturbations are assumed at freestream Mach and angle of attack as shown in Table 9. Coupling with Optimal Latin Hypercube Design (Optimal LHD) for sampling, the NIPC method is adopted to quantify the surface heating uncertainty under perturbations.

To determine the appropriate order for polynomial chaos, comparison was made between surface thermal uncertainty features quantified from second-order and third-order PCEs constructed at each surface point, as shown in Fig. 16. The researched surface thermal uncertainties include the mean value and the standard deviation under perturbations. The mean value was used to describe the average situation of aerodynamic thermal performance under freestream disturbance, while the standard deviation was to represent the variation. The second-order PCE is built using the Optimal LHD samples set in Table 10. The third-order PCE is built utilizing a different 18 samples set designed from Optimal LHD, which is not shown here, however. The calculation state was set at the baseline condition in Table 3 with perturbations described in Table 9. It is observed that the contours of the surface heat flux mean value and standard deviation under order 2 and 3 are similar respectively, which means that order convergence of the NIPC method is achieved. After that, as displayed in Table 11, uncertainties in the same gauging points as before are compared between the second-order NIPC results and the arithmetic values of the same samples in Table 10. It can be summarized that the NIPC results are approximate to the arithmetic values.

On account of that, the second-order NIPC method is sufficient and computing-resources saving, and will be applied in the inner-layer in the following part to describe the aerodynamic thermal uncertainty. The outer-layer will utilize the ANOVA method to analyze the jet design factors on surface thermal uncertainty.

6.3.1. Parameters study on surface heat flux uncertainty

As the same with subsection 6.2, parameters sensitivity on surface heat flux uncertainty are firstly researched in this subsection. Results are shown in Fig. 17 and Fig. 18 below.

Similar to the baseline freestream condition ($Ma = 6$, $\alpha = 0°$, Fig. 12), the parameter that has the largest influence on the mean heat flux is D, up to 65% to 75%. The next important are PR and T_{oj}, which are all 'extremely significant' factors. Although the effect of δ is 'significant' and even 'extremely significant' at some gauging points, it is still only little influential, no more than 5%. L/D is a 'not significant' factor on the mean heat flux.

The influence of D, which is an 'extremely significant' factor, on the standard deviation of surface heat flux is still the largest. PR is the second important factor, which can be 'extremely significant' at some local measuring points. The other three parameters have little influence and are 'not significant' factors. Among them, although T_{oj} reaches a 'significant' effect at the measuring points of 60° and 70°, it still has only a weak influence of about 5%. After 70°, the influences of all the parameters have been reduced to some extent. These parameters even become 'not significant' when θ is equal to 90°.

Table 9
Freestream disturbance information.

Disturbance source		Basic value	Disturbance range	Distribution
Freestream Mach number	Ma_∞	6	±10%	*Uniform*
Freestream angle of attack (deg.)	α	0	±5	*Uniform*

Table 10
Sample set for 2-order NIPC method.

Sample	Ma_∞	α/(deg.)	Sample	Ma_∞	α/(deg.)
1	5.95	−1.36	7	6.60	−0.45
2	5.62	5.00	8	6.27	0.45
3	5.73	−4.09	9	6.49	3.18
4	5.84	2.27	10	6.05	−5.00
5	6.16	4.09	11	6.38	−3.18
6	5.51	1.36	12	5.40	−2.27

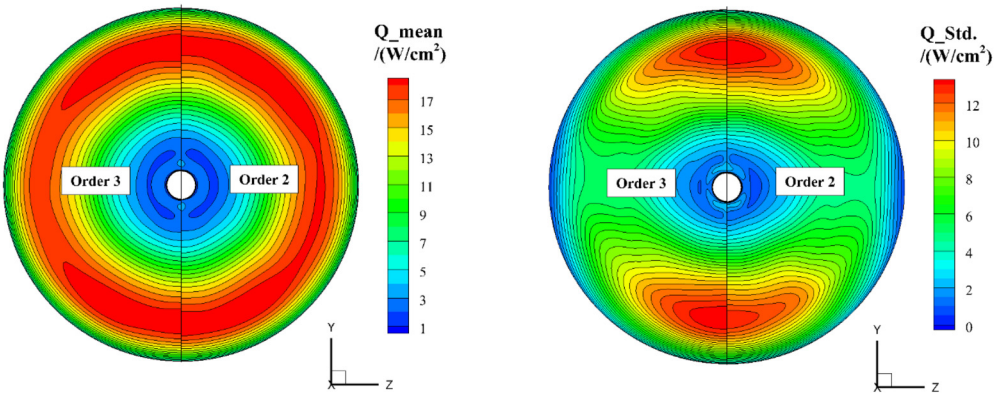

Fig. 16. Comparisons of heat flux uncertainty features between NIPC methods of order 2 and 3. (Mean value: left; Standard deviation: right).

Table 11
Comparison between NIPC results and arithmetic values of samples.

		10°	20°	30°	40°	50°	60°	70°	80°	90°
Mean value (W/cm^2)	NIPC	2.35	4.79	10.81	15.99	18.65	17.46	13.09	8.35	4.73
	Arithmetic	2.64	5.06	11.26	16.47	19.19	17.75	13.20	8.41	4.75
	Err	−10.98%	−5.34%	−4.00%	−2.91%	−2.81%	−1.63%	−0.83%	−0.71%	−0.42%
Standard deviation (W/cm^2)	NIPC	1.49	4.61	8.97	11.77	13.40	11.22	7.56	4.57	2.57
	Arithmetic	2.02	5.49	10.63	13.88	15.78	13.08	8.64	5.14	2.88
	Err	−26.24%	−16.03%	−15.62%	−15.20%	−15.08%	−14.22%	−12.50%	−11.09%	−10.76%

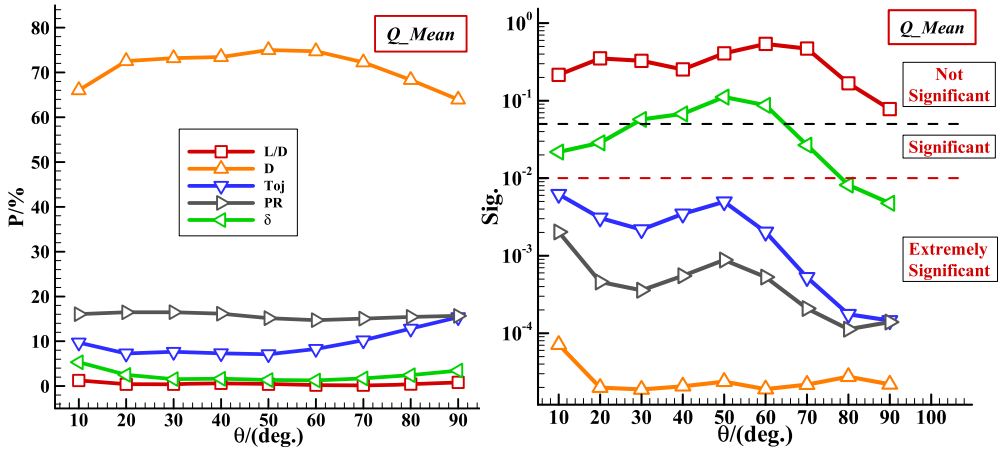

Fig. 17. Parameters sensitivity on the mean value of surface heat flux under uncertainty.

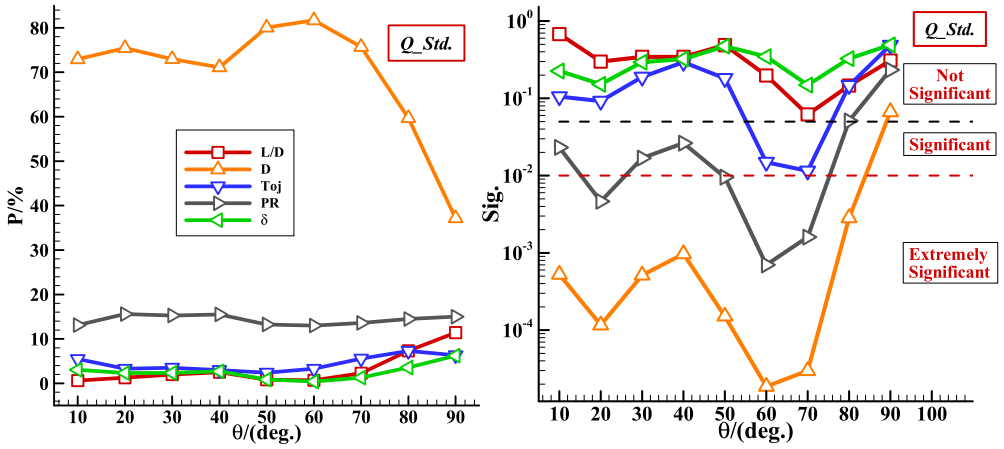

Fig. 18. Parameters sensitivity on the standard deviation of surface heat flux under uncertainty.

Table 12
Parameters study on surface total heat load uncertainty under incoming disturbance.

		L/D	D	T_{oj}	PR	δ
$P/\%$	Mean	0.20	70.38	9.37	16.90	2.73
	Std.	7.71	18.29	6.44	7.32	31.79
$Sig.$	Mean	0.38561	0.00003	0.00040	0.00010	0.00680
	Std.	0.54800	0.28857	0.59842	0.56562	0.15354

It is indicated that D, PR, and T_{oj} have important effects on the mean surface heat flux under perturbations, which is similar to that in baseline condition. While those of δ and L/D are weak and can be ignored. When interests are turned to the standard deviation, which is the key variable in robust optimization and represents variation of surface heating, it can be drawn that only D and PR have important influences, with others 'not significant'. It means that, when performing robust optimization of adding appropriate reversed-jet at the tip for aerodynamic heat reduction of blunt-shape vehicles, only the nozzle entry diameter, the total-pressure ratio of jet-to-freestream, as well as the nozzle entry total temperature need to be focused to get satisfactory results.

6.3.2. Parameters study on surface total heat load uncertainty

This subsection will exert research on influences of the jet design parameters on uncertainty of surface total thermal load under incoming disturbance. With comparison between Table 8 and Table 12, conclusion can be summarized that parameters influence on the mean surface total heat load under disturbance and that of the baseline condition are almost the same, with only δ more significant under perturbations. When interests are turned to the standard deviation of surface total thermal load, it can be found that the variation of the thermal load is small under perturbations, and all of the jet parameters become 'not significant', although not same with that of the mean value.

7. Conclusions

Two-layers research structure is developed in current paper to investigate the jet design parameters on surface thermal uncertainty of a blunt body under free incoming perturbations. In the inner layer, the Non-Intrusive Polynomial Chaos method is used to quantify surface thermal uncertainty caused by freestream perturbations in Mach number and angle of attack. In the outer layer, the Analysis of Variance method is applied to reveal the influence and significance of the jet design parameters on surface thermal uncertainty. Previous to this, results of three different single-and-determinate free incoming conditions are compared to show the difference of the jet parameters influence on surface heating. Conclusions are summarized as below:

(1) The change of Mach number is found to be able to result in different influence and significance of jet design parameters on surface heat flux and total heat load.
(2) The change of angle of attack is found to be able to result in different influence and significance of jet design parameters on surface heat flux at leeward, however little difference at windward. Besides, the total heat load also changes little under the variation of angle of attack.
(3) When perturbations occurred in freestream Mach number and angle of attack, surface heating varied, and uncertainty thus emerged at the surface thermal property. Parameters sensitivity on the mean value of surface heat flux are similar with that under baseline free incoming condition, with D, PR and T_{oj} all greatly influential and extremely significant. However, only D and PR perform crucially for the standard deviation of surface heat flux, the effect of T_{oj} is no longer significant, with others neglected. For that of surface total heat load, although factors impacts are all different from those before, they are all insignificant in virtue of little variation on total heat load.
(4) Researches on the influences of the jet parameters on surface thermal uncertainty are helpful to grasp the key jet factors on aerodynamic thermal control under a wide range of freestream conditions more accurately, and could provide useful information for robust optimization on the reverse jet.

Declaration of competing interest

We declare that we have no financial and personal relationships with other people or organizations that can inappropriately influence our work, there is no professional or other personal interest of any nature or kind in any product, service and/or company that could be construed as influencing the position presented in the manuscript entitled, "*Reverse jet parameters study on aerodynamic thermal uncertainty of a blunt body*".

Acknowledgements

This work was supported by grants from the National Natural Science Foundation of China (No. 11721202). Moreover, the first author, W Zhang would like to sincerely thank FZ Zeng and FJ Cai from Beihang University for their assistance in reviewing this article.

References

[1] Zhao Yatian, Yan Chao, Liu Hongkang, Qin Yupei, Assessment of laminar-turbulent transition models for hypersonic inflatable aerodynamic decelerator aeroshell in convection heat transfer, Int. J. Heat Mass Transf. 132 (2019) 825–836.

[2] H.B. Lu, W.Q. Liu, Investigation on thermal protection efficiency of hypersonic vehicle nose with forward-facing cavity, J. Astronaut. 33 (8) (2012) 1013–1018.

[3] W.A. Engblom, D.B. Goldstein, D. Ladoon, et al., Fluid dynamics of hypersonic forward-facing cavity flow, J. Spacecr. Rockets 34 (4) (1997) 437–444.

[4] P.J. Finley, The flow of a jet from a body opposing a supersonic free stream, J. Fluid Mech. 26 (1966) 337–368.

[5] Y. Kim, T. Roh, H. Huh, H. Jin, Study on the combined effect of various injection conditions on the drag reduction by a counter-flow jet in supersonic flow, Aerosp. Sci. Technol. 1 (2019) 105580.

[6] B.X. Shen, W.Q. Liu, L. Yin, Drag and heat reduction efficiency research on opposing jet in supersonic flows, Aerosp. Sci. Technol. 77 (2018) 696–703.

[7] S. Srinath, K.P.J. Reddy, Experimental investigation of the effects of aerospike geometry on aerodynamic drag and heat transfer rates for a blunt body configuration at hypersonic Mach numbers, Int. J. Hypersonics 1 (2) (2010) 93–114.

[8] J. Huang, W.-X. Yao, N. Qin, Heat reduction mechanism of hypersonic spiked blunt body with installation angle at large angle of attack, Acta Astronaut. 164 (2019) 268–276.

[9] S. Mohandas, R. Krishna Siddharth, B. John, Reduction of wave drag on parameterized blunt bodies using spikes with varied tip geometries, Acta Astronaut. 160 (2019) 25–35.

[10] J. Huang, W.X. Yao, Multi-objective design optimization of blunt body with spike and aerodisk in hypersonic flow, Aerosp. Sci. Technol. 93 (2019) 105122.

[11] F. Deng, F. Xie, N. Qin, W. Huang, L. Wang, H. Chu, Drag reduction investigation for hypersonic lifting-body vehicles with aerospike and long penetration mode counterflowing jet, Aerosp. Sci. Technol. 76 (2018) 361–373.

[12] W. Sheng, Z. Wei, C. Fangjie, W. Qiang, Y. Chao, Uncertainty and sensitivity study on blunt body's drag and heat reduction with combination of spike and opposing jet, Acta Astronaut. 167 (2020) 52–62.

[13] M. Barzegar Gerdroodbary, M. Imani, D.D. Ganji, Heat reduction using counterflowing jet for a nose cone with aerodisk in hypersonic flow, Aerosp. Sci. Technol. 39 (2014) 652–665.

[14] W. Huang, A survey of drag and heat reduction in supersonic flows by a counterflowing jet and its combinations, J. Zhejiang Univ. Sci. A 16 (2015) 551–561.

[15] W. Huang, Z. Chen, L. Yan, B. bin Yan, Z. bo Du, Drag and heat flux reduction mechanism induced by the spike and its combinations in supersonic flows: a review, Prog. Aerosp. Sci. 105 (2019) 31–39.

[16] X. Sun, W. Huang, M. Ou, R. Zhang, S. Li, A survey on numerical simulations of drag and heat reduction mechanism in supersonic/hypersonic flows, Chin. J. Aeronaut. 32 (2019) 771–784.

[17] Z. guo Wang, X.wan Sun, W. Huang, S. bin Li, L. Yan, Experimental investigation on drag and heat flux reduction in supersonic/hypersonic flows: a survey, Acta Astronaut. 129 (2016) 95–110.

[18] Xi-wan Sun, Wei Huang, Zhen-yun Guo, et al., Multi-objective design optimization of hypersonic combinational novel cavity and opposing jet concept, J. Spacecr. Rockets 54 (3) (2017) 662–671.

[19] J.S. Shang, J. Hayes, K. Wurtzler, et al., Jet-spike bifurcation in high-speed flows, AIAA J. 39 (6) (2001) 1159–1165.

[20] Y.Y. Zheng, N. Ahmed, A Novel Means of Dissipation of Shock Wave Induced Heat in a High Speed Flow, AIAA Fluid Dynamics Conference, 2013.

[21] B. Meyer, H.F. Nelson, D.W. Riggins, Hypersonic drag and heat-transfer reduction using a forward-facing jet, J. Aircr. 38 (2001) 680–686.

[22] K. Hayashi, S. Aso, Y. Tani, Experimental study on thermal protection system by opposing jet in supersonic flow, J. Spacecr. Rockets 43 (2006) 233–236.

[23] K. Hayashi, S. Aso, Y. Tani, Numerical study on aerodynamic heating reduction by opposing jet, Mem. Fac. Eng., Kyushu Univ. (2006) 66.

[24] Takashige Imoto, Hisashi Okabe, Shigeru Aso, et al., Enhancement of Aerodynamic Heating Reduction in High Enthalpy Flows with Opposing Jet, AIAA, 2011, 2011-346.

[25] Bo Li, Numerical Simulation and Analysis of Opposing Jet Flow Field, PhD thesis, Harbin Engineering University, Harbin, 2014 (in Chinese).

[26] R. Sriram, G. Jagadeesh, Film cooling at hypersonic Mach numbers using forward facing array of micro-jets, Int. J. Heat Mass Transf. 52 (15–16) (2009) 3654–3664.

[27] M. Barzegar Gerdroodbary, M. Imani, D.D. Ganji, Investigation of film cooling on nose cone by a forward-facing array of micro-jets in hypersonic flow, Int. Commun. Heat Mass Transf. 64 (2015) 42–49.

[28] J. Guo, G. Lin, X. Bu, et al., Parametric study on the heat transfer of a blunt body with counterflowing jets in hypersonic flows, Int. J. Heat Mass Transf. 121 (2018) 84–96.

[29] Zhao Yatian, Yan Chao, Liu Hongkang, Zhang Kailing, Uncertainty and sensitivity analysis of flow parameters for transition models on hypersonic flows, Int. J. Heat Mass Transf. 135 (2019) 1286–1299.

[30] Zhao Yatian, Yan Chao, Wang Xiaoyong, Liu Hongkang, Uncertainty and sensitivity analysis of SST turbulence model on hypersonic flow heat transfer, Int. J. Heat Mass Transf. 136 (2019) 808–820.

[31] J. Blazek, Computational Fluid Dynamics: Principles and Applications, second ed., Elsevier Ltd., Oxford, 2005.

[32] F.R. Menter, Two-equation eddy-viscosity turbulence models for engineering applications, AIAA J. 32 (8) (1994) 1598–1605.

[33] C.L. Rumsey, Compressibility considerations for k-ω turbulence models in hypersonic boundary layer applications, NASA/TM-2009-215705, 2009.

[34] Shi-bin Li, Zhen-guo Wang, George N. Barakos, et al., Research on the drag reduction performance induced by the counterflowing jet for waverider with variable blunt radii, Acta Astronaut. 127 (2016) 120–130.

[35] Li Shi-bin, Wang Zhen-guo, Huang Wei, et al., Effect of the injector configuration for opposing jet on the drag and heat reduction, Aerosp. Sci. Technol. 51 (2016) 78–86.

[36] Shi-bin Li, Zhen-guo Wang, Wei Huang, et al., Drag and heat reduction performance for an equal polygon opposing jet, J. Aerosp. Eng. 30 (1) (2017) 04016065.

[37] Shi-bin Li, Zhen-guo Wang, Wei Huang, et al., Analysis of flowfield characteristics for equal polygon opposing jet on different freeflow conditions, Acta Astronaut. 133 (2017) 50–62.

[38] A. Bueno-Orovio, C. Castro, F. Palacios, E. Zuazua, Continuous adjoint approach for the Spalart-Allmaras model in aerodynamic optimization, AIAA J. 50 (2012) 631–646.

[39] Peter A. Gnoffo, James Weilmuenster, Robert D. Braun, et al., Influence of sonic-line location on Mars pathfinder probe aerothermodynamics, J. Spacecr. Rockets 33 (2) (1996) 169–177.

[40] Veronika V. Tyurenkova, Lyuben I. Stamov, Flame propagation in weightlessness above the burning surface of material, Acta Astronaut. 159 (June 2019) 342–348.

[41] V.V. Tyurenkova, M.N. Smirnova, Material combustion in oxidant flows: self-similar solutions, Acta Astronaut. 120 (2016) 129–137.

[42] K. Zhong, C. Yan, S. sheng Chen, X. yong Wang, S. jun Ju, Numerical study on the aerothermodynamics of different heatshield configurations for Mars entry capsules, Acta Astronaut. 157 (2019) 189–198.

[43] Xi-wan Sun, Zhen-yun Guo, Wei Huang, et al., A study of performance parameters on drag and heat flux reduction efficiency of combinational novel cavity and opposing jet concept in hypersonic flows, Acta Astronaut. 131 (2017) 204–225.

[44] M. Ou, L. Yan, W. Huang, S. Li bin, L. Li quan, Detailed parametric investigations on drag and heat flux reduction induced by a combinational spike and opposing jet concept in hypersonic flows, Int. J. Heat Mass Transf. 126 (2018) 10–31.

[45] R. rui Zhang, W. Huang, L. Yan, L. quan Li, S. bin Li, R. Moradi, Numerical investigation of drag and heat flux reduction mechanism of the pulsed counterflowing jet on a blunt body in supersonic flows, Acta Astronaut. 146 (2018) 123–133.

[46] W. Huang, W.D. Liu, S. Bin Li, Z.X. Xia, J. Liu, Z.G. Wang, Influences of the turbulence model and the slot width on the transverse slot injection flow field in supersonic flows, Acta Astronaut. 73 (2012) 1–9.

[47] W. Huang, M. Pourkashanian, L. Ma, D.B. Ingham, S. Bin Luo, Z.G. Wang, Effect of geometric parameters on the drag of the cavity flameholder based on the variance analysis method, Aerosp. Sci. Technol. 21 (2012) 24–30.

[48] W. Huang, J. Liu, L. Yan, L. Jin, Multiobjective design optimization of the performance for the cavity flameholder in supersonic flows, Aerosp. Sci. Technol. 30 (2013) 246–254.

[49] W. Huang, Z.G. Wang, D.B. Ingham, L. Ma, M. Pourkashanian, Design exploration for a single expansion ramp nozzle (SERN) using data mining, Acta Astronaut. 83 (2013) 10–17.

[50] W. Huang, Design exploration of three-dimensional transverse jet in a supersonic crossflow based on data mining and multi-objective design optimization approaches, Int. J. Hydrog. Energy 39 (2014) 3914–3925.

[51] M. Ou, L. Yan, W. Huang, T. tian Zhang, Design exploration of combinational spike and opposing jet concept in hypersonic flows based on CFD calculation and surrogate model, Acta Astronaut. 155 (2019) 287–301.

[52] L. Li quan, W. Huang, L. Yan, Z. Du bo, M. Fang, Numerical investigation and optimization on the micro-ramp vortex generator within scramjet combustors with the transverse hydrogen jet, Aerosp. Sci. Technol. 84 (2019) 570–584.

[53] S. Ju, C. Yan, X. Wang, et al., Effect of energy addition parameters upon scramjet nozzle performances based on the variance analysis method, Aerosp. Sci. Technol. (2017) S1270963817312452.

[54] Y.P. He, Design of Experiment and Analysis, third ed., Chemical Industry Press, Beijing, 2012, pp. 46–48 (in Chinese).

[55] Yann Caniou, Bruno Sudret, Distribution-based global sensitivity analysis using polynomial chaos expansions, Proc., Soc. Behav. Sci. 2 (2010) 7625–7626.

[56] Ju. Shengjun, Yan Chao, Ye Zhifei, Multi-parameter sensitivity analysis of air-breathing hypersonic vehicle, J. Beijing Univ. Aeronaut. Astronaut. 43 (5) (2017) 927–935 (in Chinese).
[57] S. Hosder, R.W. Walters, M. Balch, Efficient sampling for non-intrusive polynomial chaos applications with multiple uncertain input variables, in: 48th AIAA/ASME/ASCE/AHS/ASC Structures, Structural Dynamics, and Materials Conference, Honolulu, Hawaii, April 2007, pp. 23–26.
[58] John D. Anderson Jr., Fundamentals of Aerodynamics, fourth ed., McGraw-Hill Education, New York, 2007.
[59] Xiaoyong Wang, Chao Yan, Weilin Zheng, et al., Laminar and turbulent heating predictions for Mars entry vehicles, Acta Astronaut. 128 (2016) 217–228.
[60] N.N. Smirnov, V.B. Betelin, V.F. Nikitin, L.I. Stamov, D.I. Altoukhov, Accumulation of errors in numerical simulations of chemically reacting gas dynamics, Acta Astronaut. 117 (2015) 338–355.
[61] N.N. Smirnov, V.B. Betelin, R.M. Shagaliev, V.F. Nikitin, I.M. Belyakov, Yu.N. Deryuguin, S.V. Aksenov, D.A. Korchazhkin, Hydrogen fuel rocket engines simulation using LOGOS code, Int. J. Hydrog. Energy 39 (2014) 10748–10756.